Enhanced Oxidation Stability of Transparent Copper Films Using a Hybrid Organic-Inorganic Nucleation Layer

P. Bellchambers[1], M. Walker[2], S. Huband[2], A. Dirvanauskas[1] and R. A. Hatton[1*]

[1]Department of Chemistry, University of Warwick, Coventry, CV4 7AL, UK.

[2]Department of Physics, University of Warwick, Coventry, CV4 7AL, UK.

*Ross.Hatton@warwick.ac.uk

Abstract

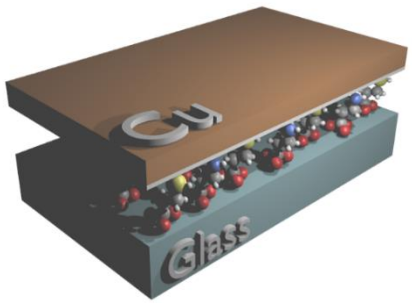

We report a novel seed layer for the formation of slab-like transparent copper films on glass and plastic substrates, based on a mixed molecular monolayer and an ultra-thin (0.8 nm) aluminium layer both deposited from the vapour phase, which substantially outperforms the best nucleation layer for optically thin copper films reported to date. Using this hybrid layer, the metal percolation threshold is reduced to < 4 nm nominal thickness and the long-term stability of sub-10 nm films towards oxidation in air is comparable to that of silver films of the same thickness fabricated using the best reported seed layer for optically thin silver films to date. The underlying reason for the remarkable effectiveness of this hybrid nucleation is elucidated using a combination of photoelectron spectroscopy, small angle X-ray studies, atomic force microscopy and transmission electron microscopy.

Introduction

Despite their current dominance, it is clear that an alternative to the transparent conducting oxides indium tin oxide (ITO), fluorine doped tin oxide and aluminium doped zinc oxide is required as the window electrode for flexible and low cost optoelectronic devices including organic photovoltaics (OPVs).[1,2] Metal films with a thickness of 6-10 nm deposited by vacuum evaporation are a promising contender because they are chemically well-defined and compatible with flexible substrates, whilst also offering high electrical conductivity and very low surface roughness.[1] Additionally, vacuum evaporation is established as a low-cost large-scale production method for the deposition of thin metal films that is compatible with roll-to-roll processing.[3] Lithographic patterning of thin metal films and/or using wide band gap anti-reflecting interlayers enables sufficient far-field transparency for metal film electrodes to be competitive with ITO glass for the same sheet resistance.[4–8]

Until now, silver (Ag) has been the favoured base metal for this purpose due to its low optical losses and highest electrical conductivity amongst metals.[9] However, Ag is a costly metal and so its use in large area, low cost applications would necessitate recovery and re-use of the metal.[10] In recent years copper (Cu) has received growing attention as a low cost alternative to Ag for window electrode applications because it has an electrical conductivity comparable to Ag at ~1% of the cost.[11–13] It has also been shown that the higher optical losses in Cu, as compared to Ag, can be mitigated by electrode and/or device design, including using a metal oxide overlayer to increase transparency.[14–16]

Due to the high surface energy of Cu and Ag these metals interact only weakly with glass and other technologically important transparent plastic substrates, such as

polyethylene terephthalate (PET) and polyethylene naphthalate (PEN), and so the formation of robust and continuous films of these metals with thickness < 10 nm is notoriously difficult to achieve using thermal evaporation.[3,17] Metal atoms condensing on the substrate diffuse over the surface and aggregate into particles which only form a continuous network for nominal thicknesses > 10 nm.[5,18,19] To enable the formation of uniform slab-like Cu and Ag films at sub-10 nm metal thickness a variety of different inorganic and organic nucleation layers have been proposed whose primary function is to suppress metal atom diffusion during early stages of film growth.[6,17,20,21] For evaporated Cu films the most successful seed layers to date are based on the use of molecular monolayers that chemically bind both to the substrate and Cu, including 3-mercaptopropyl(trimethoxysilane) [MPTMS] and 3-aminopropyl(trimethoxysilane) [APTMS].[22–24]

Surprisingly, despite the high potential of optically thin Ag and Cu films as transparent electrodes for optoelectronic applications, studies of the long-term stability of Ag or Cu window electrodes are sparse.[24–27] Stability towards air oxidation is a particularly important consideration because oxidation of the surface of very thin metal films can have a large detrimental effect on the electrode sheet resistance, as well as forming a barrier to charge transport between the electrode and an adjacent semiconducting layer in a device.[26] In practice the substrate electrode is inevitably exposed to air during transportation, or during one or more device fabrication steps, and even with device encapsulation air gradually ingresses into the device over time; a particular challenge for achieving useful lifetimes on plastic substrates.[25]

Herein we report a novel organic-inorganic bilayer for seeding the formation of Cu films which substantially outperforms the molecular monolayer approach in terms of the percolation threshold for Cu films, and dramatically improves the long-term stability towards oxidation in air. The hybrid layer is based on a mixed molecular monolayer (MM) deposited from the vapour phase followed by an ultra-thin (0.8 nm) aluminium (Al) layer. A combination of photoelectron spectroscopy, small angle X-ray studies (SAXS), atomic force microscopy and transmission electron microscopy are used to elucidate the underlying reasons for the effectiveness of this hybrid layer.

Results and Discussion

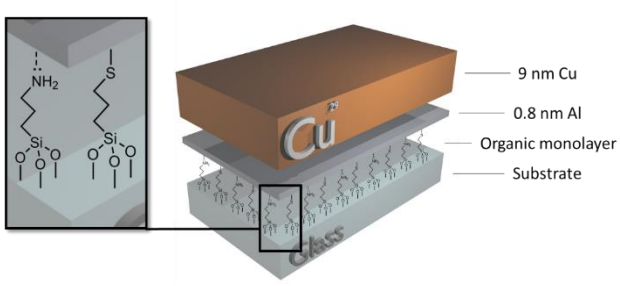

Figure 1: Schematic diagram depicting the structure of the hybrid nucleation layer and Cu electrode. The expansion (left) shows the mixed molecular monolayer bound to the substrate which can be glass (as shown) or plastic.

We have previously shown that a mixed molecular monolayer of MPTMS and APTMS co-deposited from the vapour phase is an effective seed layer for the formation of Cu films on both glass and plastic substrates.[22,23] APTMS catalyses the coupling reaction with

the substrate, while both APTMS and MPTMS bind strongly to the incoming Cu atoms as they arrive at the substrate resulting in more slab-like film formation and vastly improved film quality at < 10 nm.[3,22,24,28] Using this approach the surface roughness of a 9 nm evaporated Cu film on glass is reduced from 1.44 ± 0.12 to 1.02 ± 0.05 nm and the initial sheet resistance is reduced from 13.8 to 10.8 Ω sq^{-1}.

Due to the very low metal thickness the sheet resistance is a sensitive probe of oxidation of optically thin Cu films in air.[15,23,29] The oxidation of Cu in air is not a self-limiting process and results in the formation of a mixture of the short-lived hydroxide ($Cu(OH)_2$) and stable oxides (Cu_2O and CuO), all of which have a conductivity at least six orders of magnitude lower than the base metal.[30–34] It is evident from Figure 2 that using a mixed APTMS/MPTMS seed layer reduces the rate of oxidation of a 9 nm Cu film on glass by a factor of 4 from 0.0198 to 0.0048 Ω sq^{-1} hr^{-1}. This large improvement in stability can be rationalized in terms of the more compact slab-like structure of the Cu film deposited onto seed layer modified glass, which impedes the diffusion of oxygen along the grain boundaries between crystallites.[24]

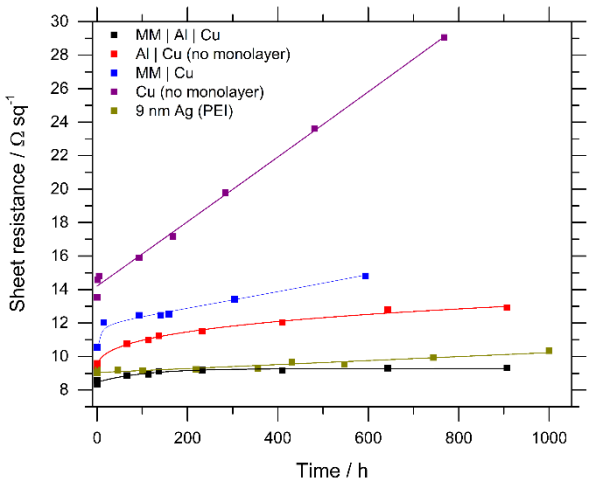

Figure 2: Evolution of the sheet resistance for representative electrodes in air for 6 electrode structures. All Al layers are 0.8 nm thick and all Cu layers 9 nm thick for comparison. The fitted lines are to 'guide the eye' only. The corresponding electrode structures are given in full in SI Table S1. SI, Figures S1 and S2 show the complete data sets for all electrode structures. The temperature and humidity fluctuated in the range 18-30°C and 15-50% respectively during testing.

The stability of the films towards oxidation in air is dramatically improved by a factor of ~ 8 from 0.0198 to 0.0026 Ω sq^{-1} hr^{-1} over those deposited directly on glass with the inclusion of the 0.8 nm Al layer alone, as compared to a ~4× increase for the organic seed layer. Crucially, the beneficial effects are additive and so by using the organic monolayer in conjunction with the Al nucleation layer improves stability by > 37× to 0.0005 Ω sq^{-1} hr^{-1}. This stabilizing effect is also achieved on flexible plastic substrates (SI, Figures S3 and S4). Remarkably the rate of oxidation of the Cu film with a buried Al layer is comparable to that achieved using an Al or Ni deposited to the top surface of the Cu film.[24,35] Also

included in Figure 2 is the evolution of the sheet resistance of a 9 nm Ag film fabricated using a polyethylenimine (PEI) adhesion layer, which serves as a benchmark against which the stability of the Cu films can be judged, since optically-thin Ag films supported on PEI modified plastic substrates are the best performing Ag film electrodes to date.[3,5]

We have previously shown that an ultra-thin (0.8 nm) Al layer deposited onto the top-surface of a Cu film is an extremely effective means of passivating thin Cu films towards oxidation in air because the Al diffuses to the grain boundaries where it oxidizes to form a plug towards oxygen ingress.[24] To investigate the possibility that the improved stability stems from a proportion of the buried Al diffusing along grain boundaries in the Cu to the surface of the film where it could form an oxide barrier to oxidants, we have used X-ray photoelectron spectroscopy to probe for Al at the surface before and after 400 hours air-oxidation (SI, Figure S5). Based on the inelastic electron mean-free path of photoelectrons ejected from the Al 2s orbital (binding energy: 119.3 eV) it is estimated that 95% of the signal is derived from the top 6 nm of the electrode (3λ).[36] The absence of a peak that can be assigned to Al is therefore compelling evidence that the Al remains confined to the interface between the Cu and the mixed monolayer.

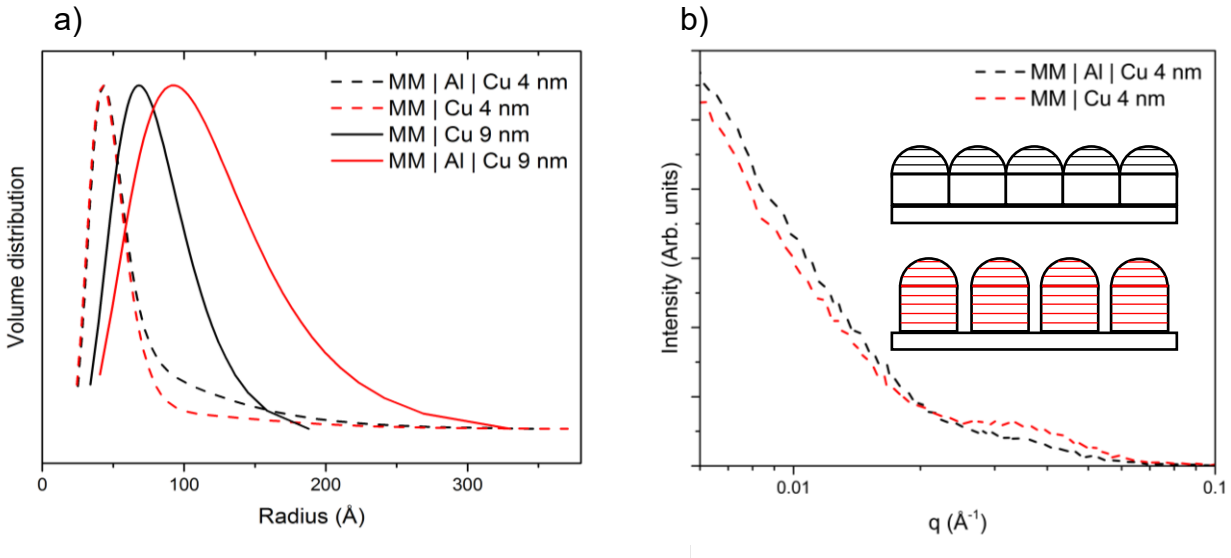

Figure 3: The results of a Small-Angle X-ray Scattering (SAXS) study. a) The outputs of a simplified model fitting the SAXS data of the electrodes as prepared, where the polycrystalline structure is modelled as a monolayer of spherical particles (SI, Figure S6). b) The raw SAXS data for the early-stage (4 nm) Cu films. (Inset) A simplified depiction of the difference between the Cu film structure with (black) and without (red) the 0.8 nm Al layer, with the volume sampled by SAXS lined. The slab-like nature of these polycrystalline films is well established on the molecular monolayer,[24] and confirmed on the hybrid nucleation layer reported here by TEM in SI, Figure S7.

To gain insight into why the hybrid layer is more effective than the molecular nucleation layer alone at seeding Cu film formation, small-angle X-ray scattering (SAXS) was used to determine the size distribution of the Cu crystallites both for a Cu film thickness of 9 nm and 4 nm deposited onto a glass derivatized with a molecular

monolayer, with and without an 0.8 nm Al seed layer.[37–39] It is evident from Figure 3 (a) that for a Cu thickness of 4 nm (i.e. in the early stage of film formation) the mean horizontal crystallite radius is comparable with and without the 0.8 nm Al. However, the much less pronounced hump in intensity in Figure 3 (b) indicates that the surface roughness of the 4 nm Cu film supported on hybrid layer is significantly reduced, consistent with a more compact metal film having a smaller volume that can be sampled by SAXS (illustrated in Figure 3 (b)).

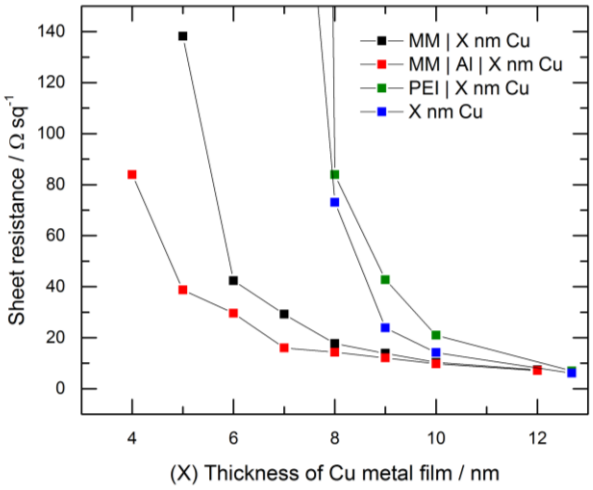

Figure 4: A comparison of the effect that reducing the Cu film thickness has on the sheet resistance for a series of nucleation layers.

When the Cu thickness is increased to 9 nm there is a doubling of the size of the Cu crystallites formed on the hybrid adhesive later, that does not occur for films on the molecular seed layer. This large increase in crystallite size is indicative of fusing together of the smaller Cu crystallites to form larger crystallites which is consistent with the lower

root-mean-square (RMS) surface roughness of 9 nm Cu films on the 0.8 nm Al layer (0.93 ± 0.03 nm, SI Figure S8) as compared to the mixed monolayer alone (1.02 ± 0.01 nm). (SI, Figure S8). The onset of this process of coalescence is expected to occur for lower metal thicknesses when the isolated particles are more densely packed crystallites. This conclusion is corroborated by the much lower percolation threshold for electrical conductivity for Cu films supported on the hybrid seed layer (Figure 4): It is evident from the correlation between sheet resistance and metal thickness in Figure 4 that the hybrid layer is remarkably effective as a nucleation layer for evaporated Cu films on glass, reducing the percolation threshold substantially below that of either the mixed molecular adhesive layer or Al seed layer. For example, at 5 nm Cu thickness the sheet resistance is 39 Ω sq^{-1}. This reduction in the percolation threshold is also evident from the fact the Cu films on the hybrid nucleation layer retain their red colouration for thickness below 6 nm (SI, Figures S9 and S10). Without the 0.8 nm Al layer Cu films with thickness ≤7 nm have a dark coloration, which is due to excitation of localised surface plasmons associated with a particulate film morphology. (SI, Figure S9). Notably, although PEI is effective as a nucleation layer for optically thin Ag films it is clear from Figure 4 that it is not a good nucleation layer for optically thin Cu films on glass because the onset of percolation occurs at a comparable thickness to that achieved on glass without a nucleation layer. These data collectively show that the improvement in stability towards air-oxidation correlates with the larger mean Cu crystallite size. It is reasonable to expect that oxygen diffuses most easily along grain boundaries between crystallites, as compared to directly into the crystallites, and so boundaries between grains will be

particularly susceptible to oxidation in air.[24] Increasing the mean crystallite size reduces the density of grain boundaries, and thus the susceptibility of the film to oxidation in air.

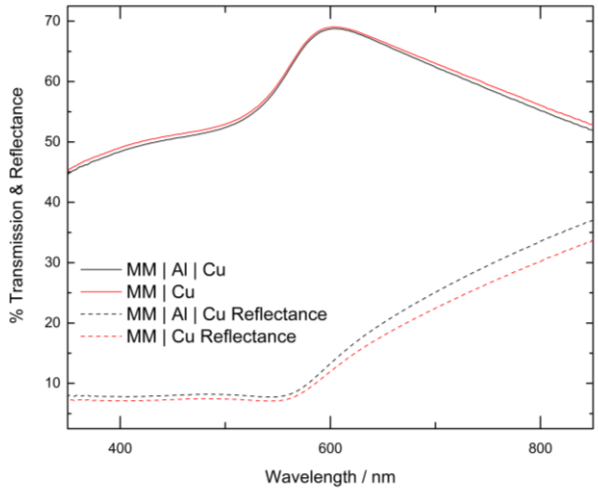

Figure 5: The UV-vis spectra of four comparable electrodes based upon a 9 nm Cu film (0.8 nm Al layer where stated). A glass reference was used to subtract the reflection from the substrate/air boundary to reflect that this is greatly reduced in commercial applications when using anti-reflective coatings.

Figure 5 shows the effect of the thin metallic seed layer on the transmittance of the Cu-based electrode. The additional reflectance caused by the very thin aluminium seed layer is offset by suppression of the parasitic absorption due to surface plasmonic excitations, and so far-field transparency is not degraded as might ordinarily be expected when using a metallic seed layer.[17]

Conclusion

In summary, a monolayer of 3-mercaptopropyl(trimethoxysilane) and 3-aminopropyl(trimethoxysilane) together with an 0.8 nm Al layer is shown to be a remarkably effective seed layer for the formation of slab-like evaporated copper films on glass and plastic substrates. The ultra-thin Al layer is deposited immediately prior to copper evaporation in the same vacuum. This hybrid seed layer outperforms the best nucleation layer for copper films reported to date in two key respects: (1) by reducing the metal percolation threshold to < 4 nm nominal thickness without incurring additional optical loses; (2) by dramatically improving the long term stability of sub-10 nm copper films towards oxidation in air, such that the stability is comparable to that of silver films of the same thickness fabricated using the best reported seed layer for optically thin silver films to date. The remarkable effectiveness of this hybrid nucleation layer is attributed to an increase in the Cu mean crystallite size when using this hybrid seed layer, which reduces the density of Cu grain boundaries – that part of the film most susceptible to oxidation.

Experimental Section

(Customised SPECTROS system integrated with N2 glovebox, Kurt. J. Lesker)

Electrode preparation

Glass microscope slides (7525 M, J. Melvin Freed Brand) or PET substrates were ultra-sonically agitated for 15 minutes each in diluted surfactant (Hellmanex III, Hellma Analytics), deionised water and propan-2-ol (AnalaR, VWR). These substrates were then UV/O_3 treated for 15 minutes immediately prior to use. Where stated, these slides were transferred to a dessicator and held at approx. 50 mBar for 4 hours with an open vial of mixed APTMS/MPTMS. All substrates were then transferred to the evaporator for Al, Cu or Ag deposition using a base pressure of < 5 $\times 10^{-8}$ mbar unless stated. Al was evaporated at a rate of 0.1 $Å s^{-1}$, while Cu and Ag were evaporated at 1 $Å s^{-1}$. Thicknesses were calibrated using an Asylum Research MFP-3D AFM and monitored using quartz-crystal microbalances. Masks were exchanged where required by a series of transfer arms without breaking the vacuum. During metal deposition, the chamber pressure rose to approximately 5 × 10^{-7} mbar**.** For the Ag electrodes, two nucleation layers were compared (SI, Figure S1). Polyethylenimine (PEI) was spin-cast onto freshly cleaned and UV/O_3 treated substrates (5000 rpm) from a 0.3% wt. aqueous solution and dried in air (110°C, 20 mins). Separate cleaned and UV/O_3 treated substates were heated at 120°C overnight in a loosely sealed container together with 4 drops of MPTMS.

Sheet resistance evolution

25 × 25 mm substrates were used to evaporate an electrode onto which silver contacts were painted to connect a Keithley 2400 source meter. Resistances were calculated using

the Van der Pauw method and an applied voltage of 5 mV. Electrodes were stored in ambient laboratory air and re-measured periodically. The temperature fluctuated between 18-30°C and the humidity between 15-50%.

UV-vis spectroscopy

A PerkinElmer Lambda 1050 UV/Vis spectrophotometer was used with reflectivity measured using an Integrating sphere where given. The effect of the 0.8 nm Al nucleation layer on transparency, as well as the effect of altering the percolation thickness is given in SI, Figures S9 and S10.

AFM images

An Asylum Research MFP3D instrument was used in tapping mode to map the surface of the electrodes and calculate the root mean square (RMS) roughness. For roughness measurements, a 10 × 10 μm area was mapped and an area free of interference selected for a detailed scan.

X-ray photoelectron spectroscopy (XPS)

Surface compositional and chemical state analysis was carried out using X-ray photoelectron spectroscopy (XPS) measurements conducted on a Kratos Axis Ultra DLD spectrometer at the University of Warwick Photoemission Facility. The air-exposed samples were mounted on to a standard sample bar using electrically conductive carbon tape and loaded into the instrument. Samples kept under an inert atmosphere were mounted on to Cu stubs using conductive carbon tape inside a nitrogen glovebox. The stubs were then loaded in to a vacuum transfer unit filled with nitrogen and transported to the XPS laboratory and loaded in such a manner that samples were under a nitrogen

atmosphere throughout. XPS measurements were performed in the main analysis chamber, with the sample being illuminated using a monochromated Al Kα X-ray source. The measurements were conducted at room temperature and at a take-off angle of 90° with respect to the surface parallel. The core level spectra were recorded using a pass energy of 20 eV (resolution approx. 0.4 eV), from an analysis area of 300 mm x 700 mm. The spectrometer work function and binding energy scale of the spectrometer were calibrated using the Fermi edge and $3d_{5/2}$ peak recorded from a polycrystalline Ag sample prior to the commencement of the experiments. The data were analysed in the CasaXPS package, using Shirley backgrounds and mixed Gaussian-Lorentzian (Voigt) lineshapes, with asymmetry parameters employed where appropriate. For compositional analysis, the analyser transmission function has been determined using clean metallic foils to determine the detection efficiency across the full binding energy range.

TEM images

Images in Figure S7 were collected on a Jeol 2100 LaB6 instrument. A focused ion beam (FIB) was used to prepare a thin section.

XRD SAXS

Grazing incidence small-angle X-ray scattering (GISAXS) measurements were made using a Xenocs Xeuss 2.0 equipped with a micro-focus Cu Kα source collimated with Scatterless slits. The scattering was measured using a Pilatus 300k detector with a pixel size of 0.172 mm x 0.172 mm. The detector was translated horizontally, and multiple data collections were combined creating a larger virtual detector. The distance between the detector and the sample was calibrated using silver behenate ($AgC_{22}H_{43}O_2$), giving a

value of 2.487(5) m. The magnitude of the scattering vector (q) is given by $q = 4\pi \sin\theta/\lambda$, where 2θ is the angle between the incident and scattered X-rays and λ is the wavelength of the incident X-rays. This gave a q range for the detector of 0.003 $Å^{-1}$ and 0.13 $Å^{-1}$ in the horizontal plane. This q range allows crystallite sizes between 1 and 200 nm to be determined.

Samples were aligned such that the surface was parallel to the beam and in the center of the beam. To maximize the scattering signal from the Cu layer the sample was positioned at an incidence angle (α_i) of 0.35° which is just below the critical angle of 0.4° for Cu and Cu Kα radiation. The 2d virtual detector image for the MM | Cu structure is shown in SI, Figure S6 (left). Scattering in the q_z direction (out-of-plane) is related to vertical morphology of the sample and the q_y direction (in-plane) to the horizontal morphology.

The in-plane scattering from the Cu crystallites highlighted in SI, Figure S6 (center) was integrated as a function of q producing a 1d intensity versus q data set as shown in SI, Figure S6 (center). Selecting only in-plane scattering allows the horizontal radius of the crystallites to be determined. SAXS fitting was performed in the Irena analysis package.[41] The scattering was fitted using spheres with a lognormal distribution of the radius. The fit to the measured data for the MM | Cu structure is given by the red line in SI, Figure S6 (center). When the interaction between crystallites affected the scattering a hard-sphere structure factor was included.[37, 42–44]

Supporting Information

All data supporting this study are provided as supplementary information accompanying this paper. Supporting Information is available online from the Wiley Online Library or from the author.

Acknowledgements

The authors would like to thank the United Kingdom Engineering and Physical Sciences Research Council (EPSRC) for funding (Grant numbers: EP/N009096/1 & EP/N509796/1), and Steven Hindmarsh for preparing and collecting the cross-sectional TEM images.

Conflict of Interest

The authors declare no conflict of interest.

Keywords

transparent electrode, copper, ultrathin metal film, nucleation, seed layer, passivation

References

[1] H. Lu, X. Ren, D. Ouyang, W. C. H. Choy, *Small* **2018**, *14*, 1703140.

[2] K. Ellmer, *Nat. Photonics* **2012**, *6*, 809.

[3] S. Jeong, S. Jung, H. Kang, D. Lee, S. Choi, S. Kim, B. Park, K. Yu, J. Lee, K. Lee, *Adv. Funct. Mater.* **2017**, *27*, 1.

[4] T. Gao, B. Wang, B. Ding, J. K. Lee, P. W. Leu, *Nano Lett.* **2014**, *14*, 2105.

[5] H. Kang, S. Jung, S. Jeong, G. Kim, K. Lee, *Nat. Commun.* **2015**, *6*, 6503.

[6] J. Yun, *Adv. Funct. Mater.* **2017**, *27*, 1606641.

[7] K. Sivaramakrishnan, T. L. Alford, *Appl. Phys. Lett.* **2009**, *94*, 2104.

[8] D. R. Sahu, J. L. Huang, *Appl. Surf. Sci.* **2006**, *253*, 915.

[9] D. S. Ghosh, Q. Liu, P. Mantilla-Perez, T. L. Chen, V. Mkhitaryan, M. Huang, S. Garner, J. Martorell, V. Pruneri, *Adv. Funct. Mater.* **2015**, *25*, 7309.

[10] F. C. Krebs, N. Espinosa, M. Hösel, R. R. Søndergaard, M. Jørgensen, *Adv. Mater.* **2014**, *26*, 29.

[11] J. R. Davis, Copper and Copper Alloys, ASM International, Ohio, **2001**.

[12] Nasdaq, "Nasdaq: Commodity Prices," can be found under http://www.nasdaq.com/markets/commodities.aspx, **n.d.**

[13] HKEX, "London Metal Exchange," can be found under http://www.lme.com/, **n.d.**

[14] G. Zhao, S. M. Kim, S. G. Lee, T. S. Bae, C. W. Mun, S. Lee, H. Yu, G. H. Lee, H. S. Lee, M. Song, J. Yun, *Adv. Funct. Mater.* **2016**, *26*, 4180.

[15] O. S. Hutter, R. A. Hatton, *Adv. Mater.* **2015**, *27*, 326.

[16] H. J. Pereira, J. Reed, J. Lee, S. Varagnolo, G. D. M. R. Dabera, R. A. Hatton, *Adv. Funct. Mater.* **2018**, *28*, 1802893.

[17] J. H. Im, K. T. Kang, S. H. Lee, J. Y. Hwang, H. Kang, K. H. Cho, *Org. Electron.* **2016**, *33*, 116.

[18] L. Leandro, R. Malureanu, N. Rozlosnik, A. Lavrinenko, *ACS Appl. Mater. Interfaces* **2015**, *7*, 5797.

[19] I. P. Lopéz, L. Cattin, D.-T. Nguyen, M. Morsli, J. C. Bernède, *Thin Solid Films* **2012**, *520*, 6419.

[20] N. Formica, D. S. Ghosh, A. Carrilero, T. L. Chen, R. E. Simpson, V. Pruneri, *ACS Appl. Mater. Interfaces* **2013**, *5*, 3048.

[21] J. Meiss, M. K. Riede, K. Leo, *J. Appl. Phys.* **2009**, *105*, 1.

[22] H. M. Stec, R. A. Hatton, *ACS Appl. Mater. Interfaces* **2012**, *4*, 6013.

[23] O. S. Hutter, H. M. Stec, R. A. Hatton, *Adv. Mater.* **2013**, *25*, 284.

[24] P. Bellchambers, J. Lee, S. Varagnolo, H. Amari, M. Walker, R. A. Hatton, *Front. Mater.* **2018**, *5*, 71.

[25] D. Yu, Y. Q. Yang, Z. Chen, Y. Tao, Y. F. Liu, *Opt. Commun.* **2016**, *362*, 43.

[26] A. Behrendt, C. Friedenberger, T. Gahlmann, S. Trost, T. Becker, K. Zilberberg, A. Polywka, P. Görrn, T. Riedl, *Adv. Mater.* **2015**, *27*, 5961.

[27] J. B. Kim, C. S. Kim, Y. S. Kim, Y.-L. Loo, *Appl. Phys. Lett.* **2009**, *95*, 183301.

[28] H. M. Stec, R. J. Williams, T. S. Jones, R. A. Hatton, *Adv. Funct. Mater.* **2011**, *21*, 1709.

[29] C. Zhong, Y. M. Jiang, D. M. Sun, J. Gong, B. Deng, S. Cao, J. Li, *Chinese J.*

Phys. **2009**, *47*, 253.

[30] W. Gao, H. Gong, J. He, A. Thomas, L. Chan, S. Li, *Mater. Lett.* **2001**, *51*, 78.

[31] I. Platzman, R. Brener, H. Haick, R. Tannenbaum, *J. Phys. Chem. C* **2008**, *112*, 1101.

[32] M. O'Reilly, X. Jiang, J. T. Beechinor, S. Lynch, C. NíDheasuna, J. C. Patterson, G. M. Crean, *Appl. Surf. Sci.* **1995**, *91*, 152.

[33] J. Li, J. W. Mayer, E. G. Colgan, *J. Appl. Phys.* **1991**, *70*, 2820.

[34] M. C. Biesinger, L. W. M. Lau, A. R. Gerson, R. S. C. Smart, *Appl. Surf. Sci.* **2010**, *257*, 887.

[35] D. S. Ghosh, R. Betancur, T. L. Chen, V. Pruneri, J. Martorell, *Sol. Energy Mater. Sol. Cells* **2011**, *95*, 1228.

[36] S. Tanuma, C. J. Powell, D. R. Penn, *Surf. Interface Anal.* **1994**, *21*, 165.

[37] S. Yu, G. Santoro, Y. Yao, D. Babonneau, M. Schwartzkopf, P. Zhang, S. K. Vayalil, P. Wessels, R. Döhrmann, M. Drescher, P. Müller-Buschbaum, S. V Roth, *J. Phys. Chem. C* **2015**, *119*, 4406.

[38] G. Kaune, M. A. Ruderer, E. Metwalli, W. Wang, S. Couet, K. Schlage, R. Röhlsberger, S. V Roth, P. Müller-Buschbaum, *ACS Appl. Mater. Interfaces* **2009**, *1*, 353.

[39] J. R. Levine, J. B. Cohen, Y. W. Chung, P. Georgopoulos, *J. Appl. Crystallogr.* **1989**, *22*, 528.

[40] C. Y. Ho, M. W. Ackerman, K. Y. Wu, T. N. Havill, R. H. Bogaard, R. A. Matula, S. G. Oh, H. M. James, *J. Phys. Chem. Ref. Data* **1983**, *12*, 183.

[41] J. Ilavsky, P. R. Jemian, *J. Appl. Crystallogr.* **2009**, *42*, 347.

[42] M. S. Wertheim, *Phys. Rev. Lett.* **1963**, *10*, 321.

[43] J. K. Percus, G. J. Yevick, *Phys. Rev.* **1958**, *110*, 1.

[44] E. Thiele, *J. Chem. Phys.* **1963**, *39*, 474.